Modeling the Influence of Precipitation on L-Band SMAP Observations of Ocean Surfaces Through Machine Learning Approach

Xuchen Jin, *Member, IEEE*, Xianqiang He, Palanisamy Shanmugam, Jianyun Ying, Fang Gong, Qiankun Zhu, and Delu Pan

***Abstract*—A new forward model (FM) was developed to characterize the influence of precipitation on L-band passive ocean surface measurements. The FM, which relates rain-induced brightness temperature (TB) variations to the rain rate and wind speed (WS), was established through a machine learning approach (referred to as the ML-FM). The soil moisture active passive (SMAP) data matched with integrated multisatellite retrievals for global precipitation measurement (IMERG) rain rate data and cross-calibrated multiplatform (CCMP) wind data were binned as a function of the rain rate, WS, and wind direction. The ML-FM was validated by comparing the simulated top-of-atmosphere (TOA) TB values with SMAP measurements. The results showed favorable agreement between the ML-FM outputs and SMAP data, with a root mean square error (RMSE) smaller than 0.55 K for both the horizontal and vertical polarizations. The validation results for ensuring more reasonable rainfall intensity distributions showed that the ML-FM returned stable results with a slightly reduced RMSE of ∼0.75 K for both the horizontal and vertical polarizations. Based on the ML-FM, we found that sea surface emission exhibited significant dependence on the rain rate for both polarizations. In addition, the ML-FM demonstrated signal saturation when the rain rate exceeded 45 mm/h, while precipitation slightly affected the directional characteristics of sea surface emission. These effects accounted for ∼0.3 K at a rain rate of 50 mm/h. Overall, our analyses demonstrated that the proposed ML-FM achieved superior performance in retrieving the TOA TB for both the vertical and horizontal polarizations with a higher accuracy than existing models.**

***Index Terms*—L-band, microwave remote sensing, radiometer, rain.**

Manuscript received 2 November 2023; revised 29 February 2024; accepted 11 May 2024. Date of publication 14 May 2024; date of current version 30 May 2024. This work was supported in part by the National Natural Science Foundation of China under Grant #42306199, Grant #U22B2012, Grant #U23A2037, and Grant #42176177, in part by the Zhejiang Provincial Natural Science Foundation of China under Grant #LDT23D06021D06, and in part by the Pioneer R&D Program of Zhejiang under Grant 2023C03011. *(Corresponding author: Delu Pan.)*

Xuchen Jin is with the Southern Marine Science and Engineering Guangdong Laboratory (Guangzhou), Guangzhou 510000, China, and also with the State Key Laboratory of Satellite Ocean Environment Dynamics, Second Institute of Oceanography, Ministry of Natural Resources, Hangzhou 310012, China (e-mail: jxc1993@126.com).

Xianqiang He is with the State Key Laboratory of Satellite Ocean Environment Dynamics, Second Institute of Oceanography, Ministry of Natural Resources, Hangzhou 310012, China, also with the Donghai Laboratory, Zhoushan 316021, China, also with the School of Oceanography, Shanghai Jiao Tong University, Shanghai 200030, China, and also with the Ocean College, Zhejiang University, Zhoushan 316000, China (e-mail: hexianqiang@sio.org.cn).

Palanisamy Shanmugam is with the Ocean Optics and Imaging Laboratory, Department of Ocean Engineering, IIT Madras, Chennai 600036, India (e-mail: pshanmugam@iitm.ac.in).

Jianyun Ying is with the Laboratory of Ocean Engineer, Second Institute of Oceanography, Ministry of Natural Resources, Hangzhou 310012, China (e-mail: yjyhz@aliyun.com).

Fang Gong, Qiankun Zhu, and Delu Pan are with the State Key Laboratory of Satellite Ocean Environment Dynamics, Second Institute of Oceanography, Ministry of Natural Resources, Hangzhou 310012, China (e-mail: gongfang@sio.org.cn; zhuqiankun@sio.org.cn; pandelu@sio.org.cn).

Digital Object Identifier 10.1109/JSTARS.2024.3400948

I. Introduction

THE accurate measurement of the hydrological properties of the ocean surface is essential for understanding various atmospheric and oceanographic processes and elucidating the complex dynamics of the Earth's climate system [1], [2], [3]. Recognizing their importance, remote sensing techniques, particularly L-band passive microwave remote sensing, have received considerable attention for their ability to provide frequent and global assessments of the sea surface salinity (SSS) [4], [5], wind speed (WS) [6], and storms [7], [8]. With the successful launches of the soil moisture and ocean salinity (SMOS) [9], Aquarius/SAC-D [10], and soil moisture active passive (SMAP) [11] missions, the ability of L-band radiometry for accurately measuring the hydrological properties of the ocean surface has become evident in previous studies.

Passive microwave remote sensing of sea surface properties heavily depends on the ability to successfully mitigate the influence of nontarget parameters on satellite measurements [12]. For this purpose, numerous models have been developed for determining the relationships between the observed microwave radiation and geophysical variables of interest. However, previous studies have focused mainly on modeling the effects of the WS and sea surface roughness [13], [14], [15], [16], whereas characterization of the impact of rainfall conditions on satellite measurements remains limited. Past theoretical and experimental studies have focused on evaluating specific rainfall effects, such as rain-induced seawater dilution [17], [18], rain-induced ring-wave spectra [19], [20], rain-induced local winds [21], [22], and rain-induced atmospheric attenuation [23], [24]. However, no comprehensive model exists that incorporates the main influencing factors to comprehensively assess the effects of rainfall on L-band measurements of the ocean surface. In addition, within this array of studies, the obtained conclusions differ, particularly regarding the phenomenon of rain-induced salinity dilution. The relationship between salinity anomalies

and rain rate exhibits a notable degree of variability [25]. Within the context of frequent and intense rainfall in ocean areas, it becomes vital to characterize the influence of precipitation to advance L-band passive microwave remote sensing of ocean surface properties [26].

Earlier studies based on machine learning (ML) approaches have shown considerable promise in addressing the critical need for characterizing precipitation effects. With a high computational efficiency, ML models can automatically extract features from L-band measurements through hidden layers and effectively capture complex nonlinear relationships [27]. Applying an ML approach to develop a forward model (FM) provides relative advantages over certain physics-based approaches, including coupled air–sea radiative transfer models (RTMs) [28] or two-scale rough sea surface models [29]. For instance, ML approaches offer better computational efficiency and consistency with satellite measurements [30], [31]. In addition, the ML-FM is readily adaptable to a broader range of environmental conditions as a data-driven constraint. A pertinent example is the rain impact model, which was developed under relatively low rain rates (less than 25 mm/h) and is subject to uncertainties when extrapolated to higher intensities [17], [18], [32], [33]. Given these advantages, a robust ML-based FM that can consider diverse rainfall conditions is critical for L-band measurements of ocean surfaces. This approach could also serve as a valuable reference to guide refinements in theoretical modeling approaches.

In this article, a new FM was established based on the ML approach for modeling rainfall effects on L-band radiometric measurements (referred to as the ML-FM). The data and methodology used in this study are described in Sections II and III, respectively. The model development stages and ML-FM architecture are introduced in Section IV. The model results are presented in Section V. A discussion and conclusions are provided in Sections V and VI, respectively.

II. Data

A. Data Preparation

In this study, we used several datasets to develop the ML-FM for L-band radiometry. In this section, we present a detailed description of these datasets.

1) *Satellite data:* SMAP Level 2 (L2) data obtained from the Remote Sensing System (RSS) Corporation were used in this study [34]. This publicly available SMAP L2 dataset was generated by the RSS Corporation and made available online.[1] Specifically, we extracted both horizontally and vertically polarized top-of-atmosphere (TOA) brightness temperatures (TBs) and azimuth angles along the radiometer look direction from the data records. The extracted TOA TB measurements exhibit a spatial resolution of approximately 40 km and an Earth incidence angle of approximately 40° [35]. The use of these SMAP L2 data allows leveraging the calibrated and quality-controlled TB measurements needed to develop and evaluate the ML-FM.
2) *SSS and sea surface temperature (SST) data:* SSS data were sourced from the Hybrid Coordinate Ocean Model (HYCOM) [36]. As the HYCOM provides a comprehensive three-dimensional (3-D) representation of various oceanic parameters, salinity data from the top layer were selected as model input data. Notably, the HYCOM SSS represents the bulk salinity, which is considered unaffected by precipitation. This characteristic allows the ML model to incorporate seawater dilution effects induced by precipitation in the training process. The SST is another input parameter for the ML-FM and was obtained from the Group for High-Resolution Sea Surface Temperature Sea Surface Temperature Analysis dataset (V3.0).
3) *Rain rate data:* Rain rate data were obtained from the Integrated Multi-satellitE Retrievals for global precipitation measurement (IMERG) product [37], which is provided within the SMAP Level 2 data records. The IMERG supplies global precipitation estimates at a spatial resolution of 0.1°. To match the 0.25° resolution SMAP data, a resampling procedure was applied to accordingly adjust the spatial resolution of the IMERG rain rate data. The averaged rain rate data were obtained by integrating the original IMERG data over the antenna gain using a circular Gaussian function characterized by a half-power width of 40 km.
4) *Wind speed data:* WS and direction data were obtained from the cross-calibrated multiplatform (CCMP) version 3.0 product [38], which provides wind vector estimates over the global oceans. The CCMP Level 4 (L4) data were produced by combining the measurements from various satellite microwave sensors (including QuikSCAT, SSM/I, SSMIS, TMI, GMI, AMSR-E, AMSR2, ASCAT, and WindSat) and background fields from ERA5 reanalysis 10-m neutral stable winds. The quality-controlled CCMP wind data provide the WS and direction inputs needed at resolutions aligned with the SMAP measurements.

B. Data Selection

These data were selected based on the following criteria.

1) *Eliminating land and sea ice contamination:* To mitigate potential land or sea ice contamination [39], [40], we filtered the measured TOA TB data to ensure their distance from land and polar regions. This approach also helped to minimize the influence of sidelobes and reduced the impact of radio frequency interference (RFI), providing the quality-controlled TB data necessary for developing the ML-FM for open ocean areas [41], [42].
2) *Eliminating the foam effect:* To eliminate the impact of ocean surface foam caused by high-wind conditions, TOA TB values associated with a WS value exceeding 12 m/s were excluded from the analysis. This WS filtering criterion removes TB data likely contaminated by foam under high-wind conditions, providing a quality-controlled dataset for evaluating rain effects

[1][Online]. Available at: https://data.remss.com/smap/SSS/V05.0/FINAL/L2C/

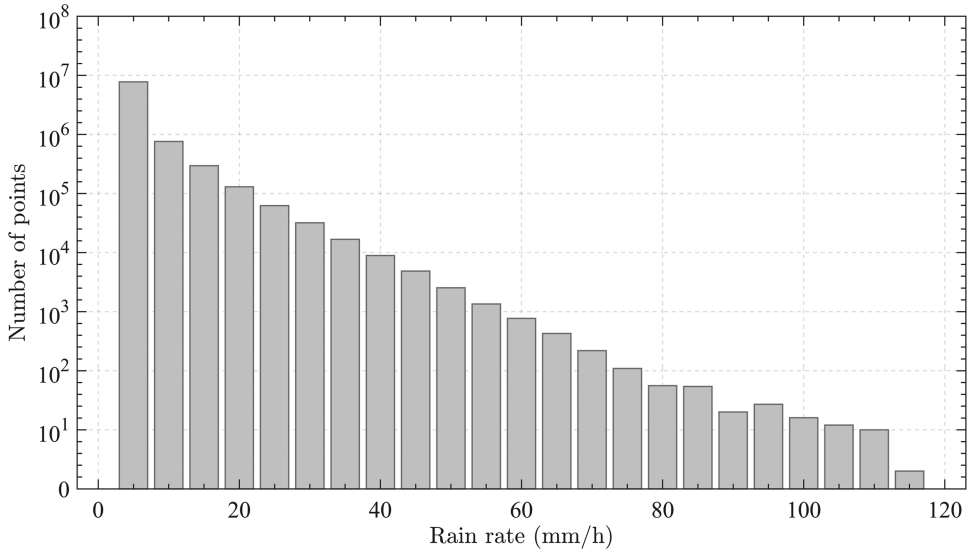

Fig. 1. Rain rate distribution of the dataset used in this study.

without the confounding influences of wind-driven foam [43].

3) *Consideration of the rainfall intensity:* Considering the negligible rainfall effects on both the sea surface and atmosphere at low intensities, only TOA TB data with rain rate values exceeding 1 mm/h were included in this study. This threshold ensured that the selected data adequately captured the significant rain-induced variations.

An additional threshold for data selection was established in this article. This threshold excludes sea surface emission variability caused by precipitation greater than 0.2 times the rain rate. This threshold was determined based on our previous studies ([24], Fig. 8) and served several purposes. First, it effectively removed a substantial proportion of measurements corresponding to very low rainfall intensities, providing a more appropriate rain rate distribution in data analysis (see Fig. 1). Second, this filtering process increased the reliability of model validation by reducing the presence of lower rain rates, which typically results in a lower implicit bias. The application of this threshold ensured a more refined dataset that is consistent with our objectives and supported the validation of our model. After applying the data selection criteria detailed above (eliminating land/ice contamination, high winds, and low rain rates), the resulting dataset comprised 9 072 401 measurements for developing the proposed ML-FM.

III. Methodology

While previous studies have demonstrated that precipitation impacts both the ocean surface and atmosphere, the precise relationship between the magnitude of these impacts (especially on the ocean surface) and the rainfall intensity remains unclear. Thus, the aim of this study was to elucidate the relationship between satellite-observed TB variations and the rainfall intensity using a data-driven approach to provide a reference for the development of theoretical models and the removal of rainfall contamination during the retrieval of sea surface parameters. Fig. 2 shows an overview of the modeling approach used to characterize the effects of precipitation on SMAP observations. Rain-contaminated SMAP measurements were first converted into sea surface emissions using an atmospheric RTM. The rain-induced excess brightness temperature (ΔT_B) was then isolated

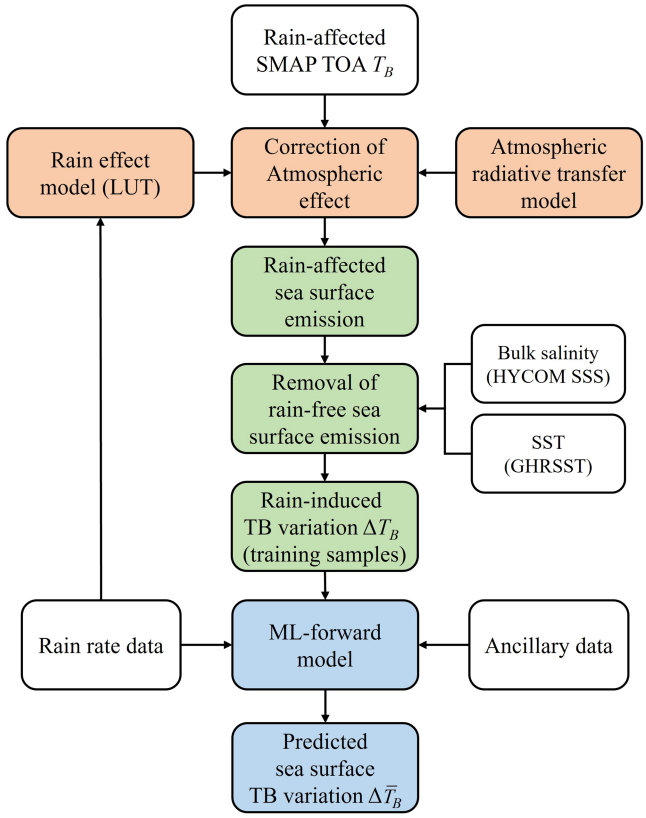

Fig. 2. Schematic visualization of the modeling process for the influence of precipitation on SMAP observations.

from these emissions and modeled using a ML approach, with HYCOM SSS values and CCMP winds as rain-free inputs. This framework facilitates the quantification of the relationship between the rainfall intensity and associated TB variations through a data-driven approach. Model development details are provided in the following sections.

According to previous studies [19], [20], [21], [22], [23], [24], precipitation impacts radiative transfer processes through the ocean surface and the overlying atmosphere. The satellite-observed TOA TB comprises contributions from sea surface emissions, atmospheric effects, and cosmic background radiation. To model these processes, we introduced a simplified radiative transfer equation for the coupled ocean–atmosphere system [44], which can be expressed as follows:

$$T_{B,\text{toa}} = T_{\text{up}} + T_B \cdot e^{-\tau} + \left(T_{\text{dw}} + e^{-\tau} \cdot T_{\text{sky}}\right) \cdot e^{-\tau} \cdot \left(1 - \frac{T_B}{\text{SST}_s}\right) + \Psi_{\text{rain}} \tag{1}$$

where $T_{B,\text{toa}}$ is the radiation at the TOA, T_{up}, and T_{dw} are the upwelling and downwelling atmospheric radiation values, respectively, T_B denotes the sea surface emission, which includes the rain effects, T_{sky} is the celestial radiation, τ is the optical depth of the atmosphere, SST_s is the sea surface temperature, and Ψ_{rain} is the correction term for the atmospheric rainfall effects.

Excluding the cosmic background radiation term, both the sea surface and atmospheric effects must be characterized for the ML-FM. However, estimating the effect of atmospheric rainfall is relatively straightforward compared to estimating complex sea surface responses. Atmospheric rainfall effects were previously modeled based on raindrop size distributions using radiative transfer theory coupled with Mie scattering calculations [24]. The RTM is often used to calculate Ψ_{rain} by propagating the L-band microwave radiation through the precipitating atmosphere [28] as follows:

$$\mu \frac{d\mathbf{L}(\tau;\mu,\phi)}{d\tau} = -\mathbf{L}(\tau;\mu,\phi) + \frac{\tilde{\omega}(\tau)}{4\pi} \int_0^{2\pi} \int_{-1}^{1} \mathbf{Z}(\tau;\mu,\phi;\mu',\phi') \cdot \mathbf{L}(\tau;\mu',\phi')\, d\mu' d\phi' + (1-\tilde{\omega})\, B(T) \tag{2}$$

where $\mathbf{L}$ is the radiant field; $\mathbf{Z}$ is the scattering matrix of the medium; μ is the cosine of the zenith angle; τ is the optical depth; φ is the azimuth angle; and $B(T)$ is the blackbody function. The matrix operator method can be used to solve this equation. By applying the matrix operator method (a detailed solution of the RTE is provided in [24], Appendix A), the atmosphere was first partitioned into 26 layers with respect to the different pressure levels according to the National Center for Environmental Prediction (NCEP) Final (FNL) Operational Global Analysis database. These layers were then subdivided into several optically thin sublayers with reflection, transmission, and internal radiation source properties denoted by the $\mathbf{R}$, $\mathbf{T}$, and $\mathbf{J}$ matrices, respectively. The two neighboring sublayers can be further combined, and the reflection ($\mathbf{R}_c$), transmission ($\mathbf{T}_c$), and source matrices ($\mathbf{J}_c$) of the combined sublayer can be obtained as

$$\begin{aligned} \mathbf{T}_c &= \mathbf{T}_2(\mathbf{E}-\mathbf{R}_1\mathbf{R}_2)^{-1}\mathbf{T}_1 \\ \mathbf{R}_c &= \mathbf{T}_2(\mathbf{E}-\mathbf{R}_1\mathbf{R}_2)^{-1}\mathbf{R}_1\mathbf{T}_2+\mathbf{R}_2 \\ \mathbf{J}_c &= \mathbf{J}_2+\mathbf{T}_2(\mathbf{E}-\mathbf{R}_1\mathbf{R}_2)^{-1}(\mathbf{J}_1+\mathbf{R}_1\mathbf{J}_2) \end{aligned} \tag{3}$$

where $\mathbf{E}$ is the identity matrix; $\mathbf{R}_i$, $\mathbf{T}_i$, and $\mathbf{J}_i$ are the reflection ($\mathbf{R}_i$), transmission ($\mathbf{T}_i$), and source matrices ($\mathbf{J}_i$), respectively, of the ith sublayer, $i = 1, 2$. By applying (3) iteratively, the thin sublayers were finally combined into a single layer, and the reflection, transmission, and source matrices of the single layer were calculated by the corresponding reflection, transmission, and internal emission properties, respectively, of the whole atmosphere. The extinction coefficients due to raindrops were calculated using Mie theory

$$\begin{aligned} K_{\text{ext}} &= \int_0^{\infty} C_{\text{ext}} n(D)\, dr \\ K_{\text{sca}} &= \int_0^{\infty} C_{\text{sca}} n(D)\, dr \end{aligned} \tag{4}$$

where K_{ext} and K_{sca} are the extinction and scattering coefficients, respectively; C_{ext} and C_{sca} are the extinction and scattering cross sections, respectively; and $n(D)$ is the Marshall–Palmer distribution used for the particle size distribution of raindrops and is given by

$$\begin{aligned} n(D) &= 8000 \exp(\lambda D) \\ \lambda &= -4.1 \cdot rr^{-0.21}\ \text{cm}^{-1} \end{aligned} \tag{5}$$

where D is the raindrop diameter. To efficiently incorporate RTM solutions into the proposed ML-FM, a look-up table (LUT) generated using RTM simulations was employed to calculate Ψ_{rain} at different rain rates.

Thus, the ML model was designed to focus solely on model calculations for the complex sea surface term. The effect of atmospheric rain was accounted for through RTM-based LUTs. This enabled the isolation of the rain-affected sea surface emission term by reformulating (1) as

$$T_B = \text{SST}_s \cdot \frac{T_{B,\text{toa}} - T_{\text{up}} - \Psi_{\text{rain}} - \left(T_{\text{dw}} + e^{-\tau} \cdot T_{\text{sky}}\right)}{\text{SST}_s - \left(T_{\text{dw}} + e^{-\tau} \cdot T_{\text{sky}}\right)} \cdot e^{\tau}. \tag{6}$$

With these values, sea surface effects could be modeled, including rain-induced effects (rain-induced ring waves, rain-induced seawater dilution, and rain-induced local winds) and wind-induced effects (roughness). For sea surface emission, the vertically and horizontally polarized TB values were obtained by the first and second Stokes parameters, respectively

$$\bar{T}_B = \begin{bmatrix} T_{Bv} \\ T_{Bh} \end{bmatrix} = \begin{bmatrix} (I+Q)/2 \\ (I-Q)/2 \end{bmatrix} \tag{7}$$

where I and Q are the first and second Stokes parameters, respectively. The excess surface TB (ΔT_B) caused by rain and wind was obtained as

$$\Delta T_B = \begin{bmatrix} \Delta T_{Bv} \\ \Delta T_{Bh} \end{bmatrix} = \begin{bmatrix} T_{Bv} - T_{Bv,\text{flat}}(S_s, T_s, \theta) \\ T_{Bh} - T_{Bh,\text{flat}}(S_s, T_s, \theta) \end{bmatrix} \tag{8}$$

where $T_{B,\text{flat}}$ is the TB for the flat sea surface, which can be calculated by the dielectric constant model [45].

According to a previous study [46], the horizontally and vertically polarized TBs (or the first and second Stokes parameters, respectively) of the sea surface are even functions of the azimuth angle φ. Thus, the first and second Stokes parameters can be expanded into a Fourier series of the azimuth angle (φ). This inherent symmetry enables the expansion of the excess TBs into a cosine Fourier series truncated at the second harmonic order, as follows:

$$\Delta\bar{T}_B = \begin{bmatrix} \Delta T_{Bv} \\ \Delta T_{Bh} \end{bmatrix} \cong \begin{bmatrix} T_{Bv,0} + T_{Bv,1}\cos\varphi + T_{Bv,2}\cos 2\varphi \\ T_{Bh,0} + T_{Bh,1}\cos\varphi + T_{Bh,2}\cos 2\varphi \end{bmatrix} \tag{9}$$

where ΔT_{Bp} is the polarized TB with p as either v or h, and the harmonic coefficients $T_{Bp,i}$ (S_s, T_s, θ, u, and rr) are functions of the SSS (S_s), SST (T_s), incidence angle (θ), WS (u), and rain rate (rr), respectively, where $i = 0, 1, 2$.

Subsequently, the ML approach was utilized to derive the three zero- to second-order harmonic coefficients from the L-band radiometric measurements. These coefficients are essential for developing the ML-FM, which represents the symmetric and asymmetric azimuthal variations in the rain-induced excess TB responses.

IV. Model Development

A. Model Selection

In this study, three common ML approaches—decision trees, neural networks (NNs), and support vector machines (SVMs)—were evaluated to characterize the impact of precipitation on SMAP L-band ocean surface observations. Decision tree algorithms operate by recursively splitting the data space into branches based on the input features to estimate a target output. They can mitigate overfitting through bootstrap aggregation, whereby predictions are averaged across multiple randomized decision trees. NNs approximate complex mappings between the inputs and outputs by learning an optimized set of weights and biases between connected nodes. The values of these parameters (weights and biases) are iteratively updated via the backpropagation and gradient descent methods to minimize the cost function. Finally, SVM algorithms aim to identify hyperplanes that maximally separate classes of data points, enabled by kernel functions that project inputs into higher-dimensional spaces to obtain linear decision boundaries.

These three widely used approaches were implemented on different platforms. Specifically, the decision tree method was implemented based on the LightGBM framework.[2] NN model training and optimization were performed using the PyTorch deep learning library. The SVM method was implemented with a linear kernel function using the fitrsvm function in MATLAB R2023a.

Among the considered approaches, the NN model demonstrated the best performance (see Table I). Thus, the NN method was selected to model the influence of precipitation on SMAP L-band ocean surface observations.

[2][Online]. Available at: https://github.com/microsoft/LightGBM/

TABLE I
Comparison of the Model Performance Levels of Different ML Approaches (Decision Tree, Neutral Network, and SVM)

Approach	RMSE	
	H-pol (K)	V-pol (K)
Decision tree	0.64	0.66
Neutral network	0.51	0.54
SVM	2.87	3.25

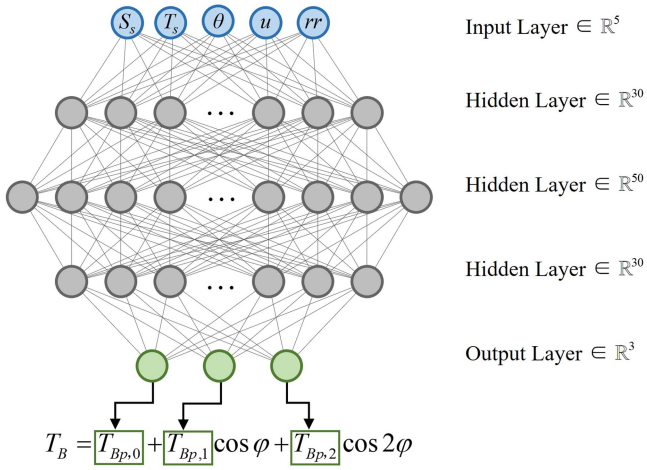

Fig. 3. Illustration of the NN model structure.

B. NN Model Setup

In contrast to conventional approaches where NNs directly predict the combined emission as a single output, the proposed model leverages the NN model to separately regress the sea surface harmonic coefficients. This represents a modification from previous NN parameterizations that output an abstract amalgamation of processes. Explicit prediction of the harmonic coefficients provides a direct link to the physical meaning of each term and allows the NN model to be interpreted through the lens of physical processes.

The proposed NN architecture includes a series of interconnected layers consisting of an input layer, three hidden layers, and an output layer (as shown in Fig. 3). In this configuration, the input layer acquires an input dataset with m samples $D = \{(x^1, \varphi_r^1, y^1), \ldots, (x^m, \varphi_r^m, y^m)\}$, where $\boldsymbol{x}^i = (S_S^i, T_S^i, \theta^i, u^i, rr^i) \in \mathbb{R}^5, i = 1, \ldots, m$ denotes the input feature vector, $y^i \in \mathbb{R}$ denotes the sea surface emission, which can be obtained from the satellite-observed TOA TB data using (6), and φ_r^i is the relative azimuth angle between the global radiometer look direction and the wind direction. Output $\boldsymbol{u}^i = (T_{B,0}^i, T_{B,1}^i, T_{B,2}^i) \in \mathbb{R}^3$ is the harmonic coefficient vector.

The hidden layers, employing a fully connected paradigm, comprise 30, 50, and 30 neurons. In each hidden layer, every neuron applies a linear transformation to the input vector through a weight vector $\boldsymbol{W} \in \mathbb{R}^n$ and bias $b \in \mathbb{R}$, where n is the number of neurons in the previous layer. The activation of l neurons in the current hidden layer is achieved by using the parametric rectified linear unit (PReLU) activation function, which can be

expressed as follows:

$$\mathrm{PReLU}\,(x) = \begin{cases} x, & \text{if } x > 0 \\ ax, & \text{if } x \le 0 \end{cases} \tag{10}$$

where a is a learnable parameter in the training process. As a result, the output $\boldsymbol{z} \in \mathbb{R}^l$ of the jth hidden layer ($j = 1, 2, 3$) can be obtained as follows:

$$\boldsymbol{z}^{[j]} = \mathrm{PReLU}\left(\boldsymbol{W}^{[j]}\boldsymbol{z}^{[j-1]} + \boldsymbol{b}^{[j]}\right) \tag{11}$$

where $\boldsymbol{z}^{[j-1]} \in \mathbb{R}^n$ is the output of the previous layer and $\boldsymbol{W} \in \mathbb{R}^{l\times n}$ and $b \in \mathbb{R}^l$ are the weight and bias parameters, respectively, to be updated. Finally, the output layer $\hat{\mathbf{y}}$ is a linear combination of the activations of the third hidden layer

$$\hat{\mathbf{y}} = \mathrm{PReLU}\left(\boldsymbol{W}_{\text{out}}\boldsymbol{z}^{[3]} + \boldsymbol{b}_{\text{out}}\right) \tag{12}$$

where $\boldsymbol{W}_{\text{out}} \in \mathbb{R}^{3\times 30}$ and $\boldsymbol{b}_{\text{out}} \in \mathbb{R}^3$ are weight and bias parameters, respectively.

The NN model can be determined by minimizing the cost function in the training process. Since the output of the NN model is the harmonic coefficient vector $\boldsymbol{u}$, the cost function is defined by estimating the distance between the actual sea surface emission $\mathbf{y}$ and the reconstructed emission obtained by summing the predicted second-order harmonic series $\hat{\mathbf{y}}$

$$J\,(\mathbf{x}) = \frac{1}{m}\sum_{i=1}^{m} \left\|\mathbf{y} - \hat{\mathbf{y}}\,(S_s, T_s, \theta, \boldsymbol{u}, rr, \varphi_r)\right\|^2 \tag{13}$$

where $\mathbf{y}$ is an $n\times 1$ SMAP measurement vector and $\hat{\mathbf{y}}$ is the corresponding FM with the form expressed in (9). To obtain the optimal weight and bias values, the cost function was minimized using the backpropagation algorithm on the given training dataset.

The above-mentioned NN model was implemented using the dataset described in Section II. Before model training, the quality-controlled data were partitioned into distinct training and test datasets for model fitting and evaluation purposes, respectively. The training data comprised 70% of the samples randomly selected from the entire dataset, whereas the remaining 30% were used for independent testing purposes.

Before training, the weights ($\boldsymbol{W}$s) and biases ($\boldsymbol{b}$s) were initialized using the Kaiming optimization technique [47]. These parameters were then updated through a backpropagation algorithm based on the cost function gradients. To ensure effective model training, the Adam optimization algorithm was utilized to iteratively adjust the weights and biases [47]. Kaiming initialization and Adam optimization are well-established techniques that facilitate efficient convergence and achieve the optimal performance during NN training. Leveraging these methods could enable proper initialization of the model parameters and efficient navigation of the high-dimensional error surface to derive an accurate mapping from the inputs to the harmonic coefficients.

During the test phase, the optimal values of $\boldsymbol{W}$s and $\boldsymbol{b}$s were derived from the training phase and applied in the test dataset to estimate the zero- to second-order harmonic coefficients. The predicted harmonic terms were summed to reconstruct the total sea surface emission, which was compared against the satellite-derived values to evaluate the model accuracy.

V. Results

A. Overall Model Performance on the Test Dataset

The developed ML-FM was validated by comparing the modeled TOA TB with the SMAP-observed TOA TB. The ML-FM provides a direct metric for analyzing the model performance under different rain rates and geophysical conditions using matched satellite observations.

The performance of the ML-FM was assessed using the test dataset, which comprises a total of 1 814 479 matchup data. The use of statistical calculations between the ML-FM-computed and SMAP-measured TOA TB data provided insights into the root mean square error (RMSE) for both the horizontal and vertical polarizations. A direct comparison revealed a close correlation between the simulated and measured TOA TB data (see Fig. 4), with RMSE values of 0.51 and 0.53 K for the horizontal and vertical polarizations, respectively. There was a substantial improvement in the ML-FM outputs relative to the theoretical values (from our previous study), with RMSE values of 1.14 and 1.51 K for the horizontally and vertically polarized TBs, respectively. However, the ML-FM-retrieved TOA TB was underestimated at high rain rates.

There could be two reasons for the deviation of the computed TOA TB: 1) the ML-FM was trained on fewer training samples at high rainfall intensities (N<150 for rain rates higher than 80 mm/h, according to Fig. 1), and 2) the ML-FM was trained on instantaneous rain rate data, thereby failing to model the accumulated fresh water input. Moreover, although the rain rate data extended to 115 mm/h, the rain rate values above 80 mm/h are less reliable and hence were excluded from the analysis.

Fig. 5 shows histograms of the difference in the TOA TB between the ML-FM-retrieved data and SMAP measurements (i.e., SMAP minus model). For both the horizontal and vertical polarizations, the data were slightly positively skewed, although they were nearly centered at approximately zero, with standard deviations (SDs) of 0.51 and 0.53 K, respectively. This difference between the retrieved and measured TOA TB data is small, which demonstrates the robust model performance over the wide range of the test data samples.

Fig. 6 shows the mean biases (differences) and SD values of the binned data as a function of the rain rate. The mean bias between the ML-FM-retrieved TOA TB and SMAP-measured TOA TB remained close to zero for all rain rates for the horizontal polarization, but it increased sharply above 60 mm/h for the vertical polarization (for example, ~0.7 K for rain rates up to 80 mm/h). This high bias occurred due to TOA TB underestimation at very high rain rates, as previously reported. Nonetheless, the SD remained small (0.5–1.6 K up to 80 mm/h), and the FM-retrieved and SMAP-measured TOA TB data points occurred close to the 1:1 line, as shown in Fig. 4.

It should be noted that the ML-FM operated as a function of both the rain rate and WS, although the WS range was limited to less than 12 m/s. Thus, the performance of the ML-FM was analyzed over a 2-D function of the rain rate and WS. Fig. 7 shows the average values of the SMAP-measured TB data minus the ML-FM TOA TB data as a 2-D function of the rain rate and WS. Except for marginal cases with sparsely

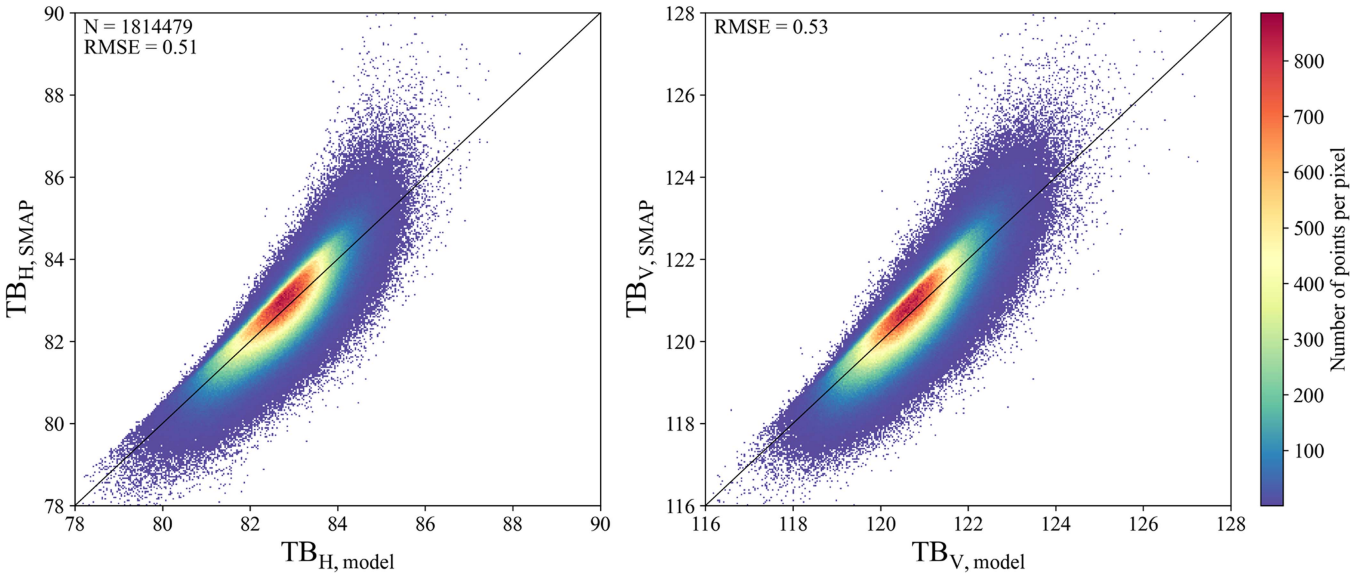

Fig. 4. ML-FM-retrieved TOA TB versus the SMAP measurement data for the horizontal (left panel) and vertical (right panel) polarizations.

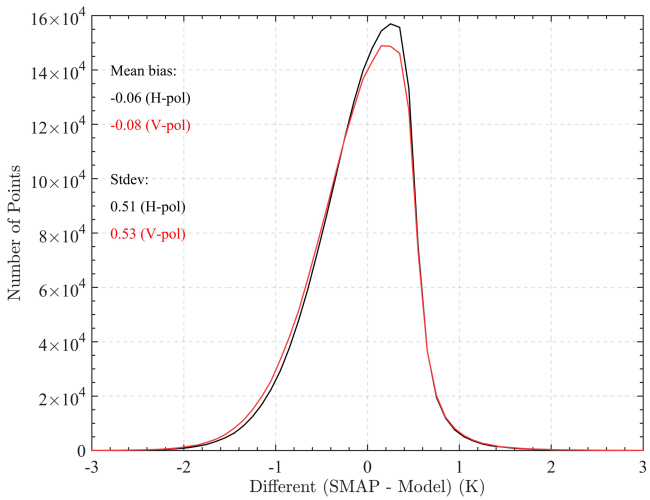

Fig. 5. Histogram of the difference between the ML-FM-retrieved TOA TB values and SMAP measurements for the test data samples.

populated data, very favorable agreement was observed between the ML-FM-retrieved TOA TB values and SMAP measurements for all RR and WS conditions (see Fig. 7). A notable exception was the horizontally polarized TB at low WSs, with a positive difference indicating underestimation of the excess emissions by the ML-FM. This highlights an area for further refinement through additional data training at low WSs and moderate rain rates.

Furthermore, the dependence of the model performance on the azimuth angle was analyzed by binning the TOA TB differences by the azimuth angle. Fig. 8 shows the mean and SD of the binned differences as a function of the azimuth angle. A suitable consistency was achieved over all azimuth angles, with a mean difference close to 0.1 K and a SD close to 1 K for both polarizations. The lack of azimuthal dependence also verified that the ML-FM could adequately learn the anisotropic rain signatures manifested at the different angles.

B. Comparison With the SMAP-GMF Data (Version 3)

The ML-FM results were compared with those of the SMAP geophysical model function (GMF) version 3.0. The SMAP-GMF model was developed by the RSS Corporation based on the retrieval algorithm for Aquarius (version 5 release) and adapted to process the SMAP data. In this analysis, RSS L-band GMF data were obtained[3] with user registration. Since the SMAP-GMF only characterizes the change in TB emitted by a rough ocean surface, the sea surface emission derived from the RSS L-band GMF was converted into the TOA TB [according to (1)] and compared with the SMAP measurements.

To evaluate the model generalization performance, SMAP measurements spanning 1 January 2022 to 31 December 2022 were utilized as an additional fully independent test set in this analysis. This one year of data was excluded from training/validation to prevent learning irrelevant temporal patterns. Although the filtering criteria described before were also applied to these data, there was still an overabundance of low rain rate cases in the data. Thus, redundant samples with low rain rates were randomly discarded to achieve a more balanced rain rate distribution (see Fig. 9). As previously noted, data with unreliable rain rates >80 mm/h were also excluded. This screening provided an unbiased 1-year evaluation dataset with a reasonably large sample size across the different rainfall conditions. A comparative assessment based on this distinct long-term dataset could quantify the actual model generalization performance.

The results shown in Fig. 10 demonstrate that the ML-FM-retrieved-TOA TB exhibited better agreement with the SMAP

[3][Online]. Available at: https://data.remss.com/smap/SSS/

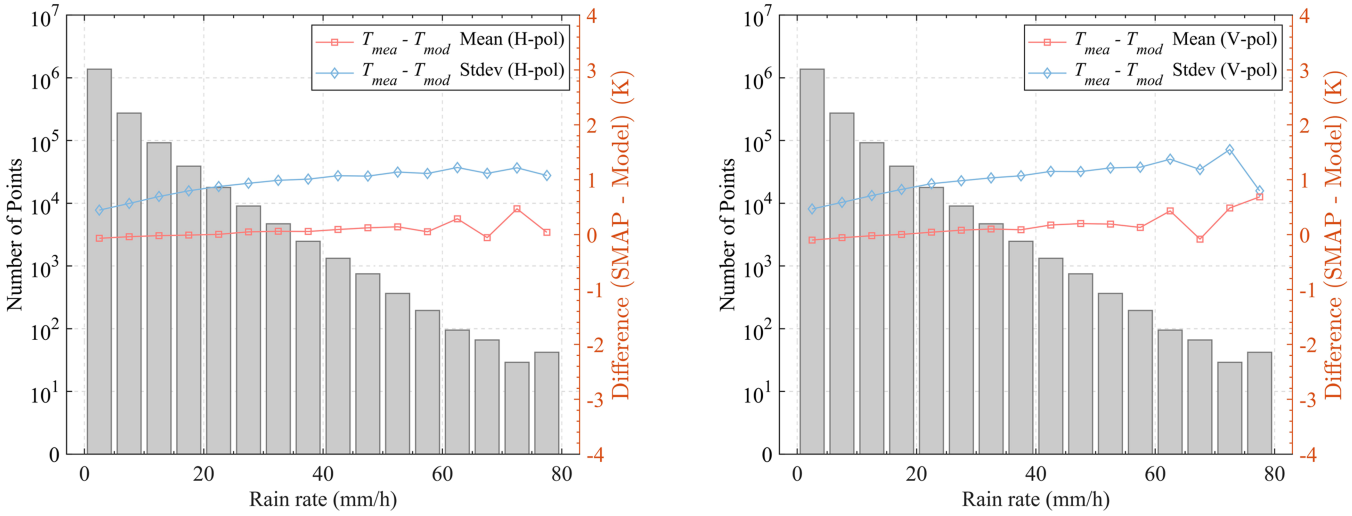

Fig. 6. Mean bias and SD of the differences between the ML-FM retrieved TOA TB values and SMAP measurement data for the horizontal (left panel) and vertical (right panel) polarizations. The bars in the background data are the rain rate histograms.

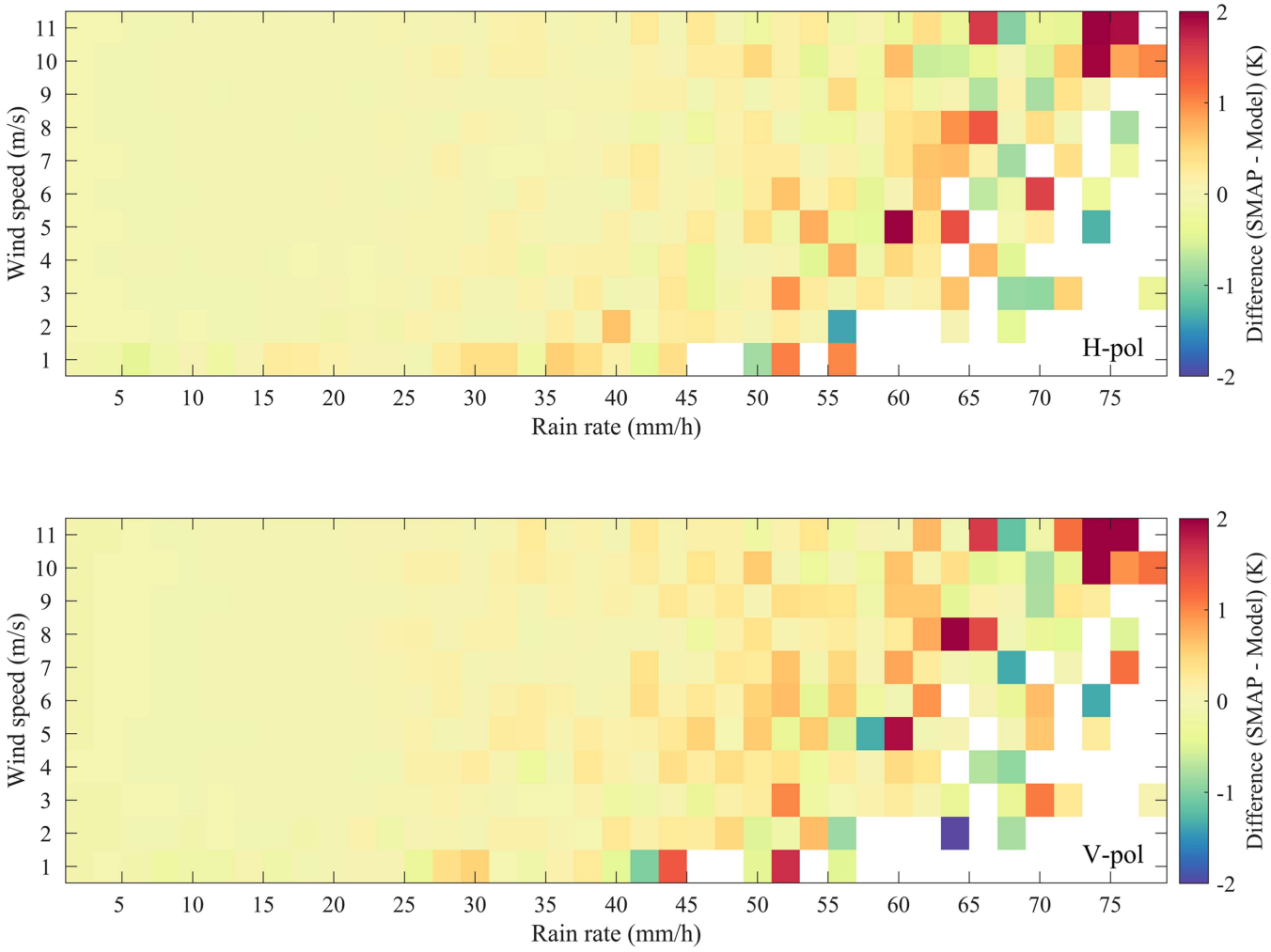

Fig. 7. Plots of the difference between the SMAP measurements and retrieved TOA TB values as a function of the rain rate and WS for the horizontal (upper panel) and vertical polarizations (lower panel). The blank array denotes no data.

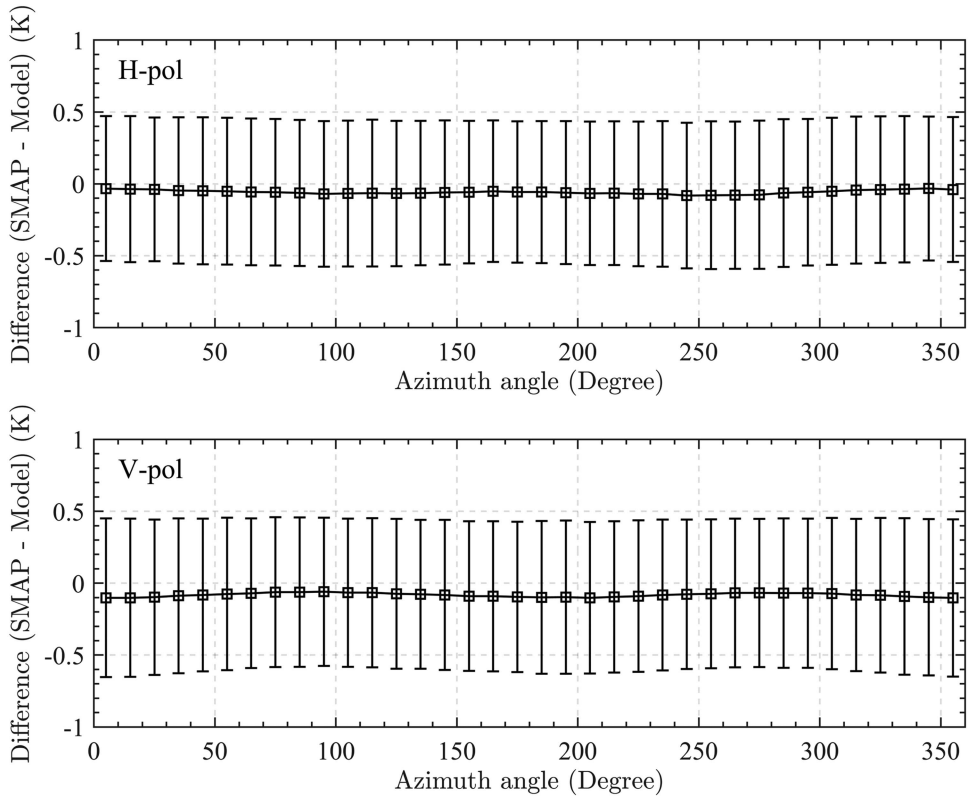

Fig. 8. Error plots (mean bias and SD) as functions of the azimuth angle for the horizontal (upper panel) and vertical (lower panel) polarizations. Bias errors (SDs) are plotted with squares (vertical bars).

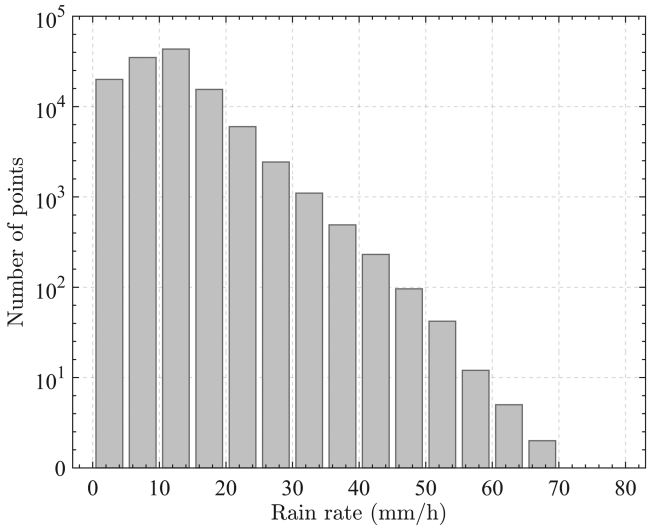

Fig. 9. Distribution of the data points for the different rain rates.

data than the RSS FM products. The superior performance of the ML-FM was indicated by RMSE values of 0.71 K for the horizontally polarized TBs and 0.73 K for the vertically polarized TBs. The RSS L-band GMF yielded RMSE values of 2.82 and 2.48 K for the horizontally and vertically polarized TBs, respectively. These findings indicated significant improvements in the TOA TB retrievals achieved by the proposed ML-FM for the different rain rates. However, the lower performance of the ML-FM on the original test dataset could be attributed to differences in the rain rate distributions. It should be noted that the original test dataset contained a high proportion of data with low rain rates, which reduced the uncertainty in TOA TB retrievals due to high rainfall intensities. Overall, our validation analysis revealed a greater accuracy of TOA TB retrieval for the proposed ML-FM than for the previous (rain effect correction) model.

Our analysis further revealed that the performance of the retrieved horizontally polarized TB products was slightly better than that of the retrieved vertically polarized TB products for both the original test data and independent 1-year data. These results are also consistent with our previous findings [24].

TABLE II
SEA SURFACE PROPERTIES FOR EXCESS SEA SURFACE EMISSION CALCULATIONS UNDER DIFFERENT RAINFALL CONDITIONS

Variables	Values (units)
SSS	34 psu
SST	290 K
WS	6 m/s

C. Model Sensitivity Analysis

The ability of the ML-FM to simulate the harmonic behavior of excess sea surface emissions under different rainfall conditions was analyzed for assimilation and retrieval applications. The sea surface properties for the model calculations are listed in Table II.

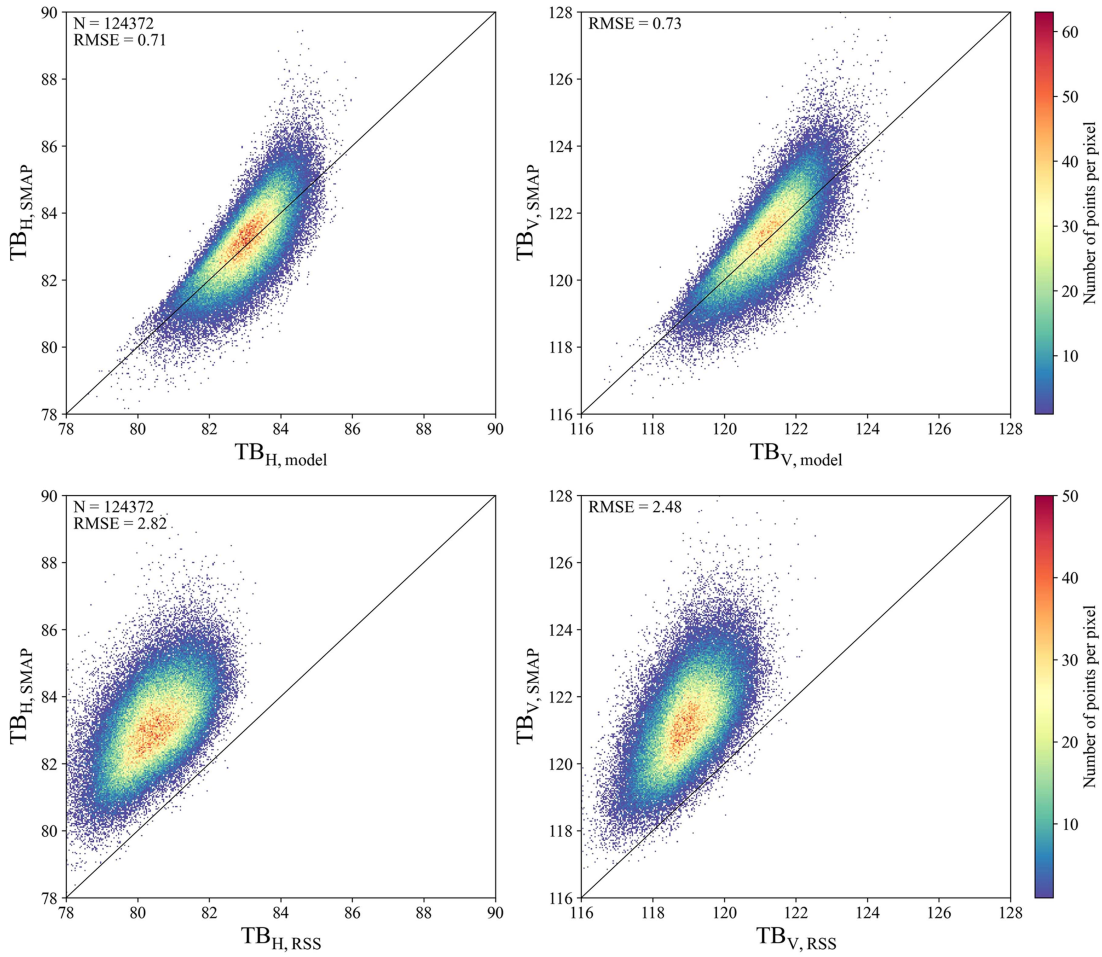

Fig. 10. Comparison of the model-retrieved TOA TB data with SMAP measurements for the horizontal (left column) and vertical (right column) polarizations for the proposed ML-FM (upper panel) and SMAP's L-band GMF (lower panel).

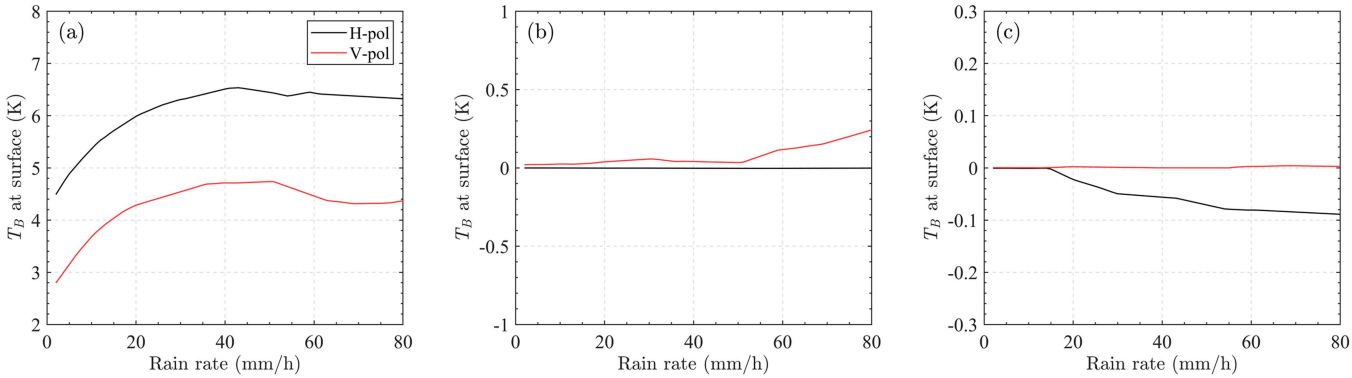

Fig. 11. (a) Zeroth-order, (b) first-order, and (c) second-order coefficients of the horizontally and vertically polarized TBs versus rainfall rates in the L-band for a sea surface temperature of 290 K, SSS of 34 psu, and WS of 6 m/s.

The ML-FM-computed zeroth-, first-, and second-order harmonic coefficients are shown in Fig. 11. As shown in Fig. 11(a), for the isotropic components ($T_{Bh,0}$ and $T_{Bv,0}$) of the excess surface emission, the horizontal polarization was slightly more sensitive to the rain rate than the vertical polarization. Moreover, the $T_{Bh,0}$ and $T_{Bv,0}$ components peaked at a rain rate of approximately 45 mm/h. There could be two reasons for these results: 1) the precipitation signal is close to saturation when the rain rate is above 50 mm/h, and 2) the model is insufficiently trained due to the insufficient data points for rain rates above 50 mm/h, so the rain effect is underestimated by the ML-FM.

The modeled first harmonic amplitudes ($T_{Bh,1}$ and $T_{Bv,1}$) [as shown in Fig. 11(b)] exhibited polarization dependence, with

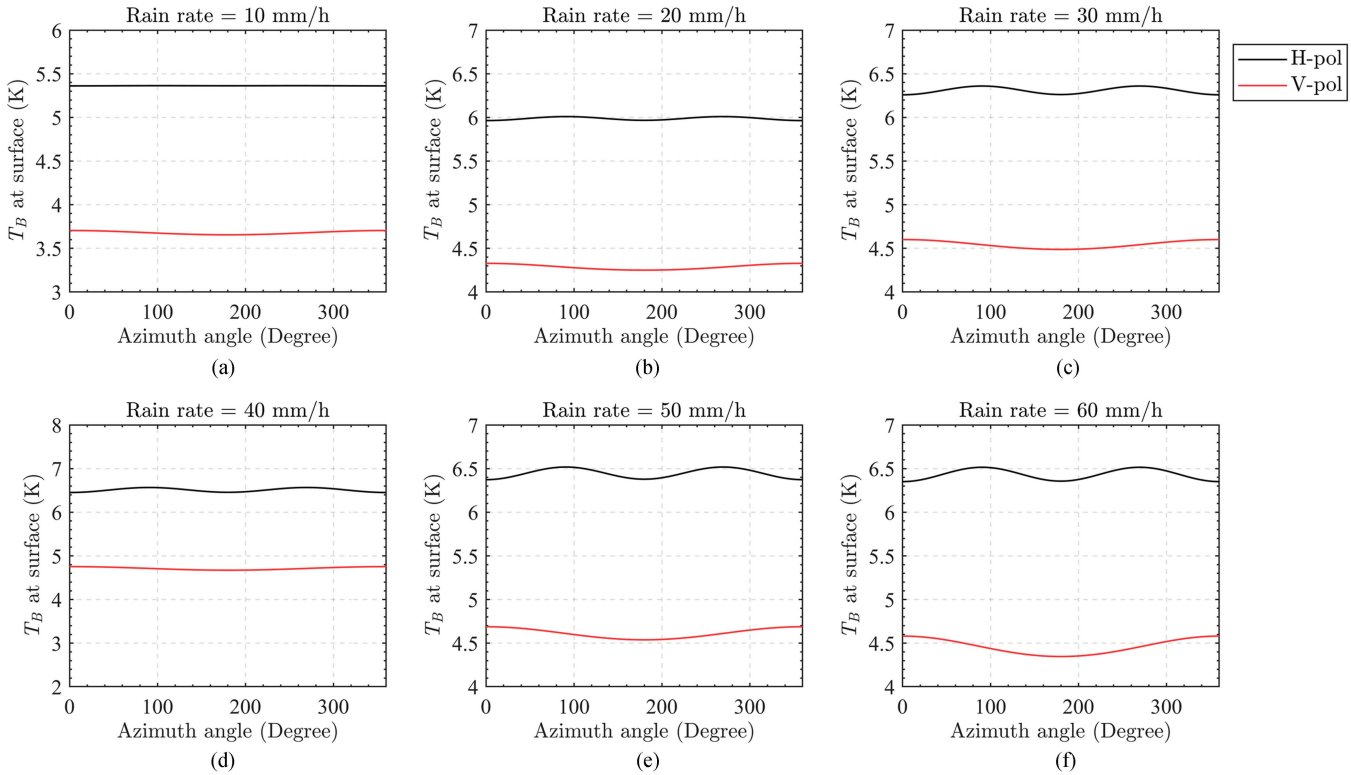

Fig. 12. Modeled excess surface emission variation as a function of the azimuth angle for six IMERG rain rates. The black and red curves denote the sums of the three-term cosine series for the horizontally and vertically polarized TBs, respectively. The sea surface properties are the same as those in Fig. 11. (a) 10 mm/h. (b) 20 mm/h. (c) 30 mm/h. (d) 40 mm/h. (e) 50 mm/h. (f) 60 mm/h.

$T_{Bv,1}$ increasing with increasing rain rate and $T_{Bh,1}$ remaining near zero. Conversely, the second harmonics ($T_{Bh,2}$ and $T_{Bv,2}$) [as shown in Fig. 11(c)] exhibited the opposite behavior, as $T_{Bh,2}$ decreased with increasing rain rate and $T_{Bv,2}$ remained approximately zero. Notably, the variations in $T_{Bh,2}$ were much lower than those in $T_{Bv,1}$. This reveals the distinct first- and second-harmonic signatures for each polarization, with the primary rainfall response manifestation in the first harmonic for the vertical polarization measurements and in the second harmonic for the horizontal polarization measurements.

Fig. 12 shows the modeled azimuthal variation in the excess surface emission for rain rates from 10 to 60 mm/h using the same sea surface properties. The peak-to-peak difference increased from nearly zero at 10 mm/h to approximately 0.3 K at 50 mm/h and above. Moreover, very similar directional patterns were obtained between the different rain rates. These results indicate that precipitation exerted a relatively minor impact on the harmonic azimuthal dependency and induced only slight perturbations to the intrinsic wind-driven directional signatures. When the amplitude of the rainfall effect increases with the rain rate, the angular shape remains largely unchanged.

D. Application of the ML-FM for SSS Retrieval

To more thoroughly assess the developed model, we employed the ML-FM to retrieve the SSS using the SMAP data for analytical purposes. However, as mentioned above, SSS retrieval analysis is qualitative rather than quantitative due to the difficulty in matching the SMAP data and in situ measurements. Therefore, a region free from the influences of land contamination, sea ice, and RFI was selected for analysis. This region occurs in the Northern Hemisphere (6°N–10°N, 122°W–126°W). According to the IMERG data, this region experienced a heavy rain event on June 11, 2021, with a maximum rain rate of 43.4 mm/h [see Fig. 13(a)]. The TB in the precipitation zone was notably elevated relative to the TB values in rain-free regions, as expected [see Fig. 13(c) and (d)]. Moreover, the surface wind in the area was relatively moderate, ranging from 0.5 to 10 m/s according to the CCMP data [see Fig. 13(b)].

It is important to emphasize that the ML-FM does not explicitly differentiate between the excess surface emission resulting from the rain-induced surface roughness and that arising from salinity dilution. Thus, we first used the previously developed model to decouple the effects of the rain-induced roughness and SSS dilution [24], after which the maximum likelihood method was employed for SSS retrieval, utilizing the specified cost function according to the RSS algorithm theoretical basis document [34], which can be defined as follows:

$$\sqrt{\chi^2} = \left\{ [T_{B,\text{surface}} - T_{B,\text{model}}]^2_{\text{V-pol}} + [T_{B,\text{surface}} - T_{B,\text{model}}]^2_{\text{H-pol}} \right\}^{0.5} \quad (14)$$

where $T_{B,\text{sur}}$ is the sea surface emission retrieved from satellite observations and $T_{B,\text{mod}}$ is the predicted TB.

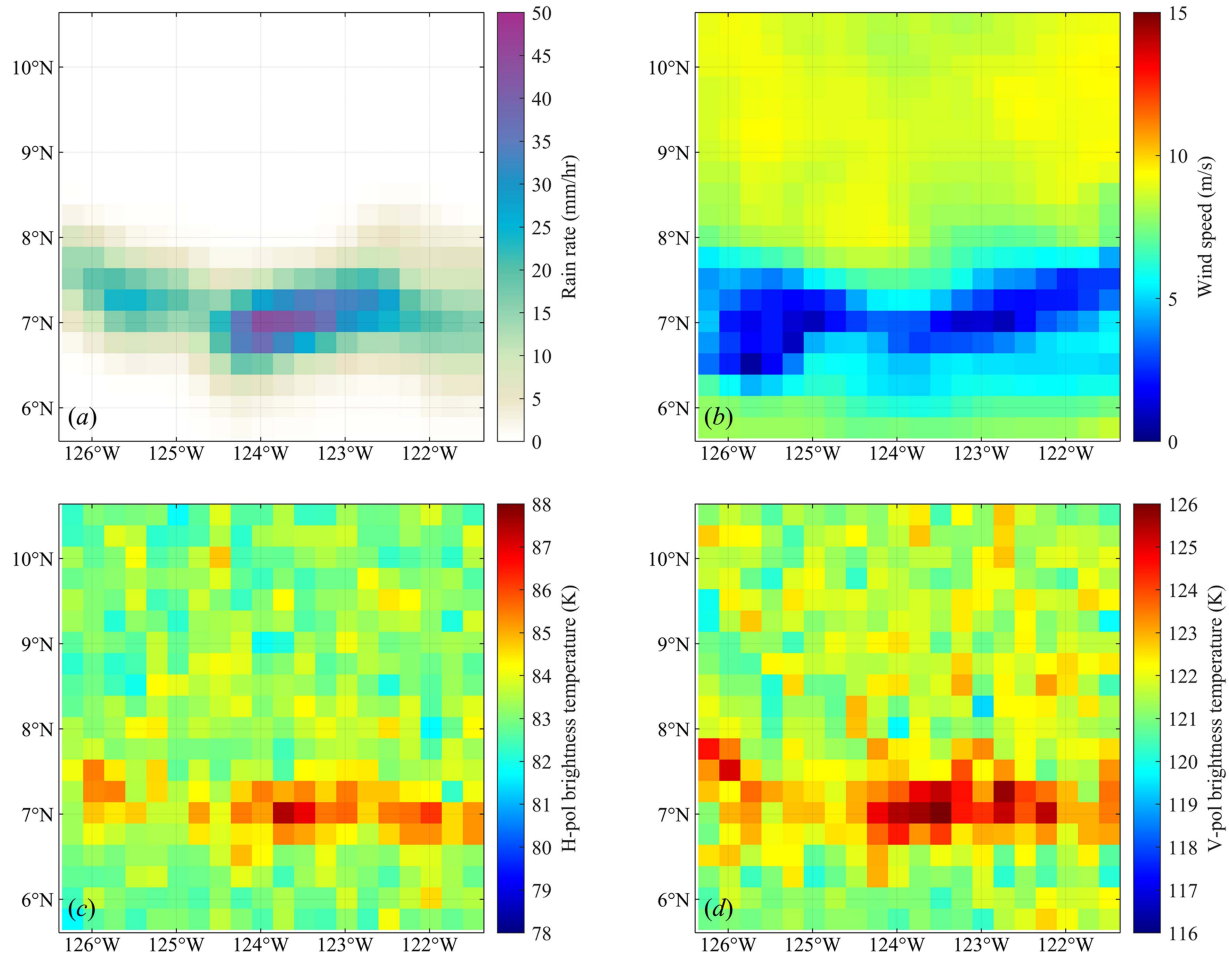

Fig. 13. Study area chosen for analysis. (a) Spatial distribution of the rain rate. (b) Spatial distribution of the WS. (c) Spatial distribution of the SMAP-observed vertically polarized TB. (d) Spatial distribution of the SMAP-observed horizontally polarized TB.

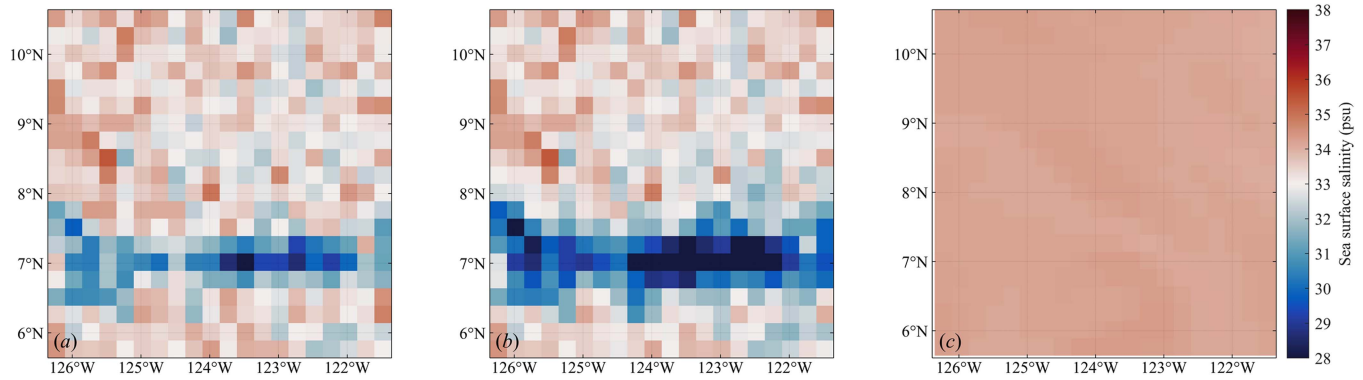

Fig. 14. Spatial distribution of the SSS. (a) With correction. (b) Without correction. (c) Reference SSS.

Consequently, Fig. 14 shows the spatial patterns of both the retrieved and reference SSS data. The retrieved SSS exhibited favorable consistency with the spatial distribution of the rain rate. The retrieved SSS without rain effect correction [see Fig. 14(b)] was much lower than that determined with the ML-FM [see Fig. 14(a)]. For example, in the area with a high rain rate (6°N–8°N, 123°W–124°W), the SSS obtained without correction was below 28 psu, whereas the corrected SSS reached approximately 31 psu. Compared to the reference SSS [depicted in Fig. 14(c)], the anomalies in the SSS induced by the rain amount reached approximately 5–6 psu, as observed in the retrieved SSS data without correction [see Fig. 14(b)]. In contrast, when the SSS was retrieved after correction, these anomalies reached approximately 3 psu. As reported in prior studies, rain-induced SSS anomalies have been estimated at approximately 1.5–3 psu at the sea surface for a rain rate of approximately 20 mm/h [17],

[25]. This suggests that in the absence of rain correction, the retrieved SSS may be underestimated.

VI. Discussion

The results described in Section V show the ability of the ML-FM to characterize the impact of precipitation on SMAP L-band ocean surface observations and validate the approach proposed in Section IV. The developed ML-FM achieved RMSE values of 0.71 K for the horizontal polarization and 0.73 K for the vertical polarization. While the accuracy is higher than that reported in a previous study [24], visual inspection of the TB distributions revealed that the ML-FM method underestimated the TB at high observed TBs (see Figs. 4 and 10). Since the WSs represented in the dataset are moderate (0–12 m/s) and the CCMP product (wind velocity and direction) exhibits a documented high accuracy relative to buoy and scatterometer measurements [48], the wind-driven sea surface roughness can be excluded as the source of model underestimation. Moreover, the order of magnitude of the difference precludes SSS and SST input data uncertainty as a likely explanation [49], [50]. Instead, the uncertainty in the precipitation input data is the primary factor contributing to the modeled underestimation. Specifically, two potential mechanisms may contribute to the observed underestimation: 1) due to the relatively small amount of low-accuracy data at very high rain rates (>45 mm/h), the proposed model may underestimate the rain-induced sea surface emission excess under these conditions and may underestimate the threshold of rainfall intensities causing signal saturation (see Fig. 11); 2) the ML-FM uses instantaneous rain rate data as input, but the excess sea surface emission induced by an accumulated freshwater input was not considered [17]. Nevertheless, this work showed that the influence of precipitation on L-band radiometer observations could be reasonably modeled.

VII. Conclusion

The use of L-band radiometers to measure ocean surface properties requires an accurate model to remove superfluous signals from the observed TBs. This requires accurate knowledge of the signal itself and its dependence on environmental factors such as the rainfall intensity and ocean surface WS. Earlier works have extensively studied wind effects within this context, but the characterization of multidimensional rainfall signatures remains very limited.

In this study, we proposed a new NN-based FM (ML-FM) to characterize L-band measurements of rain-affected ocean surfaces. Here, we first separated the atmospheric rain effect from the satellite-observed TOA TB data using the previously developed RTM. This facilitated the isolation of complex multidimensional sea surface emission signatures induced by both wind and rain. Then, we employed an NN model to predict the excess emissions of rain-affected rough sea surfaces. By learning the intricate nonlinear relationships from the data, the ML-FM could capture the effects of precipitation missing in existing models.

The ML-FM showed a significant rain rate dependence for both the horizontal and vertical polarizations. To validate the ML-FM results, we first used the test dataset. The results showed satisfactory agreement between the ML-FM-retrieved TOA TB values and SMAP measurements, with RMSE values of 0.51 and 0.53 K for the horizontal and vertical polarizations, respectively. The means and SDs of the differences (SMAP TOA TB minus modeled TOA TB) also supported these results. The mean difference was less than 1 K for all rain rates, and the SD of the differences was less than 0.6 K for rain rates lower than 60 mm/h and remained less than 1.6 K up to 80 mm/h. Furthermore, for all azimuth angles, the mean difference was close to zero, and the SD was close to 1 K. The ML-FM retrievals were then compared with the SMAP L-band FM V3 product (using SMAP data) for 2022. The results showed that the ML-FM performed better than the RSS FM when compared to the SMAP measurements under the different rainfall conditions. Consequently, the ML-FM yielded RMSE values of 0.73 and 0.71 K for the vertically and horizontally polarized TBs, respectively, which are much better than those of the RSS L-band FM (RMSE values of 2.82 and 2.48 K for the vertical and horizontal polarizations, respectively). These results clearly indicate the superior accuracy of the proposed ML-FM over that of the RSS L-band FM for correcting satellite-observed TBs under different rainfall conditions.

Finally, we evaluated the harmonic behavior and the directional characteristics of the excess surface emission. The results showed that the zeroth-order harmonic coefficients were greatly influenced by the rainfall intensity but reached a peak at a rain rate of approximately 45 mm/h. The findings also revealed that precipitation imposed relatively little effect on the directional characteristics of the excess sea surface emissions. We also applied the ML-FM (since the ML-FM cannot separate the influences of the rain-induced roughness and SSS dilution, we used our previously developed model to decouple these two parts of rain-induced sea surface effects) for SSS retrieval. The outcome revealed that the developed model effectively addresses the issue of underestimation in SSS retrieval.

Overall, the ML-FM provided a relatively satisfactory accuracy in predicting rainfall effects and could serve as a useful tool for current and future airborne and spaceborne L-band measurements of ocean surface parameters under different rainfall conditions. Moreover, the use of instantaneous rather than accumulated rain rate data represents a significant limitation that could introduce uncertainties in empirical modeling approaches, especially for prolonged and heavy precipitation events. By training on instantaneous data, the model may not fully capture rain effects over longer timescales. In the future, more efforts will be made to investigate the rain-induced sea surface emission excess under very heavy rainfall conditions and examine the dependence of the excess sea surface emission on the accumulated rain rate data for improving TB predictions by utilizing more reliable models and experimental data.

Acknowledgment

The authors would like to thank the Remote Sensing System Corporation for providing the satellite data and SMAP L-band GMF, and the SOED/SIO/MNR satellite ground station,

Satellite Data Processing Sharing Center, and marine satellite data online analysis platform (SatCO2) for their help with data collection and processing. The authors would also like thank the anonymous reviewers for their careful review and constructive suggestions that helped improve the manuscript.

REFERENCES

[1] Y. Du, Y. Zhang, and J. Shi, "Relationship between sea surface salinity and ocean circulation and climate change," *Sci. China Earth Sci.*, vol. 62, pp. 771–782, Jan. 2019, doi: 10.1007/s11430-018-9276-6.

[2] Y. Kawai and A. Wada, "Diurnal sea surface temperature variation and its impact on the atmosphere and ocean: A review," *J. Oceanogr.*, vol. 63, pp. 721–744, Oct. 2007, doi: 10.1007/s10872-007-0063-0.

[3] R. Murtugudde and A. J. Busalacchi, "Salinity effects in a tropical ocean model," *J. Geophysical Res. Oceans*, vol. 103, no. C2, pp. 3283–3300, Feb. 1998, doi: 10.1029/97JC02438.

[4] N. Reul et al., "Sea surface salinity estimates from spaceborne L-band radiometers: An overview of the first decade of observation (2010-2019)," *Remote Sens. Environ.*, vol. 242, Jun. 2020, Art. no. 111769, doi: 10.1016/j.rse.2020.111769.

[5] W. Tang et al., "Validating SMAP SSS with in situ measurements," *Remote Sens. Environ.*, vol. 200, pp. 326–340, Oct. 2017, doi: https://doi.org/10.1016/j.rse.2017.08.021.

[6] S. H. Yueh and J. Chaubell, "Sea surface salinity and wind retrieval using combined passive and active L-band microwave observations," *IEEE Trans. Geosci. Remote Sens.*, vol. 50, no. 4, pp. 1022–1032, Apr. 2012, doi: 10.1109/TGRS.2011.2165075.

[7] N. Reul, J. Tenerelli, B. Chapron, D. Vandemark, Y. Quilfen, and Y. Kerr, "SMOS satellite L-band radiometer: A new capability for ocean surface remote sensing in hurricanes," *J. Geophysical Res. Oceans*, vol. 117, no. C2, pp. 1–24, Oct. 2012, doi: 10.1029/2011JC007474.

[8] S. H. Yueh et al., "SMAP L-band passive microwave observations of ocean surface wind during severe storms," *IEEE Trans. Geosci. Remote Sens.*, vol. 54, no. 12, pp. 7339–7350, Dec. 2016, doi: 10.1109/TGRS.2016.2600239.

[9] Y. H. Kerr et al., "The SMOS mission: New tool for monitoring key elements of the global water cycle," *Proc. IEEE*, vol. 98, no. 5, pp. 666–687, May 2010, doi: 10.1109/JPROC.2010.2043032.

[10] D. M. Le Vine, G. S. E. Lagerloef, F. R. Colomb, S. H. Yueh, and F. A. Pellerano, "Aquarius: An instrument to monitor sea surface salinity from space," *IEEE Trans. Geosci. Remote Sens.*, vol. 45, no. 7, pp. 2040–2050, Jul. 2007, doi: 10.1109/TGRS.2007.898092.

[11] D. Entekhabi et al., "The soil moisture active passive (SMAP) mission," *Proc. IEEE*, vol. 98, no. 5, pp. 704–716, May 2010, doi: 10.1109/JPROC.2010.2043918.

[12] S. H. Yueh, W. Tang, A. Fore, A. Hayashi, Y. T. Song, and G. Lagerloef, "Aquarius geophysical model function and combined active passive algorithm for ocean surface salinity and wind retrieval," *J. Geophysical Res. Oceans*, vol. 119, no. 8, pp. 5360–5379, Aug. 2014, doi: 10.1002/2014JC009939.

[13] S. Soisuvarn, Z. Jelenak, P. S. Chang, S. O. Alsweiss, and Q. Zhu, "CMOD5. H—A high wind geophysical model function for C-band vertically polarized satellite scatterometer measurements," *IEEE Trans. Geosci. Remote Sens.*, vol. 51, no. 6, pp. 3744–3760, Jun. 2013, doi: 10.1109/TGRS.2012.2219871.

[14] S. H. Yueh et al., "L-band passive and active microwave geophysical model functions of ocean surface winds and applications to Aquarius retrieval," *IEEE Trans. Geosci. Remote Sens.*, vol. 51, no. 9, pp. 4619–4632, Sep. 2013, doi: 10.1109/TGRS.2013.2266915.

[15] E. V. Zabolotskikh, N. Reul, and B. Chapron, "Geophysical model function for the AMSR2 C-band wind excess emissivity at high winds," *IEEE Geosci. Remote Sens. Lett.*, vol. 13, no. 1, pp. 78–81, Jan. 2016, doi: 10.1109/LGRS.2015.2497463.

[16] H. Zhang, J. L. Garrison, R. Wijekularatne, and J. Warnecke, "A geophysical model function for S-band reflectometry of ocean surface winds in tropical cyclones," *Geophysical Res. Lett.*, vol. 46, no. 16, pp. 9843–9850, Aug. 2019, doi: 10.1029/2019GL082730.

[17] W. E. Asher, A. T. Jessup, R. Branch, and D. Clark, "Observations of rain-induced near-surface salinity anomalies," *J. Geophysical Res. Oceans*, vol. 119, no. 8, pp. 5483–5500, Aug. 2014, doi: 10.1002/2014JC009954.

[18] A. Santos-Garcia et al., "Investigation of rain effects on aquarius sea surface salinity measurements," *J. Geophysical Res. Oceans*, vol. 119, no. 11, pp. 7605–7624, Oct. 2014, doi: 10.1002/2014JC010137.

[19] L. F. Bliven, P. W. Sobieski, and C. Craeye, "Rain generated ring-waves: Measurements and modelling for remote sensing," *Int. J. Remote Sens.*, vol. 18, no. 1, pp. 221–228, Jan. 1997, doi: 10.1080/014311697219385.

[20] C. Craeye, P. W. Sobieski, and L. F. Bliven, "Scattering by artificial wind and rain roughened water surfaces at oblique incidences," *Int. J. Remote Sens.*, vol. 18, no. 10, pp. 2241–2246, Nov. 1997, doi: 10.1080/014311697217864.

[21] R. Balasubramaniam and C. Ruf, "Characterization of rain impact on L-Band GNSS-R ocean surface measurements," *Remote Sens. Environ.*, vol. 239, Mar. 2020, Art. no. 111607, doi: 10.1016/j.rse.2019.111607.

[22] D. E. Weissman et al., "Challenges to satellite sensors of ocean winds: Addressing precipitation effects," *J. Atmospheric Ocean. Technol.*, vol. 29, no. 3, pp. 356–374, Mar. 2012, doi: 10.1175/JTECH-D-11-00054.1.

[23] N. Skou and D. Hoffman-Bang, "L-band radiometers measuring salinity from space: Atmospheric propagation effects," *IEEE Trans. Geosci. Remote Sens.*, vol. 43, no. 10, pp. 2210–2217, Oct. 2005, doi: 10.1109/TGRS.2005.856115.

[24] X. Jin et al., "Impact of rain effects on L-band passive microwave satellite observations over the ocean," *IEEE Trans. Geosci. Remote Sens.*, vol. 61, pp. 1–16, Dec. 2022, doi: 10.1109/TGRS.2022.3232402.

[25] J. Boutin et al., "Satellite and in situ salinity: Understanding near-surface stratification and subfootprint variability," *Bull. Amer. Meteorological Soc.*, vol. 97, no. 8, pp. 1391–1407, 2016, doi: 10.1175/bams-d-15-00032.1.

[26] W. Tang, S. Yueh, A. Fore, G. Neumann, A. Hayashi, and G. Lagerloef, "The rain effect on Aquarius' L-band sea surface brightness temperature and radar backscatter," *Remote Sens. Environ.*, vol. 137, pp. 147–157, Oct. 2013, doi: 10.1016/j.rse.2013.06.016.

[27] Y. LeCun, Y. Bengio, and G. Hinton, "Deep learning," *Nature*, vol. 521, no. 7553, pp. 436–444, May 2015, doi: 10.1038/nature14539.

[28] X. Jin et al., "Comprehensive vector radiative transfer model for estimating sea surface salinity from L-band microwave radiometry," *IEEE Trans. Geosci. Remote Sens.*, vol. 59, no. 6, pp. 4888–4903, Jun. 2021, doi: 10.1109/TGRS.2020.3007878.

[29] S. H. Yueh, "Modeling of wind direction signals in polarimetric sea surface brightness temperatures," *IEEE Trans. Geosci. Remote Sens.*, vol. 35, no. 6, pp. 1400–1418, Nov. 1997, doi: 10.1109/36. 649793.

[30] M. Asgarimehr, I. Zhelavskaya, G. Foti, S. Reich, and J. Wickert, "A GNSS-R geophysical model function: Machine learning for wind speed retrievals," *IEEE Geosci. Remote Sens. Lett.*, vol. 17, no. 8, pp. 1333–1337, Aug. 2020, doi: 10.1109/LGRS.2019.2948566.

[31] Y. Liu, I. Collett, and Y. J. Morton, "Application of neural network to GNSS-R wind speed retrieval," *IEEE Trans. Geosci. Remote Sens.*, vol. 57, no. 12, pp. 9756–9766, Dec. 2019, doi: 10.1109/TGRS.2019.2929002.

[32] M. M. Jacob, W. L. Jones, A. Santos-Garcia, K. Drushka, W. E. Asher, and C. M. Scavuzzo, "Salinity rain impact model (RIM) for SMAP," *IEEE J. Sel. Topics Appl. Earth Observ. Remote Sens.*, vol. 12, no. 6, pp. 1679–1687, Jun. 2019, doi: 10.1109/JSTARS.2019.2907275.

[33] W. Tang et al., "Rain-induced near surface salinity stratification and rain roughness correction for Aquarius SSS retrieval," *IEEE J. Sel. Topics Appl. Earth Observ. Remote Sens.*, vol. 8, no. 12, pp. 5474–5484, Dec. 2015, doi: 10.1109/JSTARS.2015.2463768.

[34] T. Meissner et al., "NASA/RSS SMAP salinity: Version 5.0 validated release," 2022. [Online]. Available: https://data.remss.com/smap/ SSS/V05.0/documents/SMAP_NASA_RSS_Salinity_Release_V5.0.pdf

[35] T. Meissner, F. J. Wentz, A. Manaster, and R. Lindsley, "Remote sensing systems SMAP ocean surface salinities, version 5.0 validated release," 2018.

[36] E. P. Chassignet et al., "US GODAE: Global ocean prediction with the hybrid coordinate ocean model (HYCOM)," *Oceanography*, vol. 22, no. 2, pp. 64–75, Jun. 2009, doi: 10.1007/1-4020-4028-8_16.

[37] G. J. Huffman et al., "NASA global precipitation measurement (GPM) integrated multi-satellite retrievals for GPM (IMERG)," NASA Goddard Space Flight Center, Greenbelt, MD, USA, 2015.

[38] C. A. Mears et al., "A near-real-time version of the cross-calibrated multiplatform (CCMP) ocean surface wind velocity data set," *J. Geophysical Res. Oceans*, vol. 124, no. 10, pp. 6997–7010, Oct. 2019, doi: 10.1029/2019JC015367.

[39] W. Tang et al., "The potential and challenges of using soil moisture active passive (SMAP) sea surface salinity to monitor arctic ocean freshwater changes," *Remote Sens.*, vol. 10, no. 6, Jun. 2018, Art. no. 869, doi: 10.3390/rs10060869.

[40] J. Chaubell et al., "Improving brightness temperature measurements near coastal areas for SMAP," *IEEE J. Sel. Topics Appl. Earth Observ. Remote Sens.*, vol. 12, no. 11, pp. 4578–4588, Nov. 2019, doi: 10.1109/JSTARS.2019.2951323.

[41] P. N. Mohammed, M. Aksoy, J. R. Piepmeier, J. T. Johnson, and A. Bringer, "SMAP L-band microwave radiometer: RFI mitigation prelaunch analysis and first year on-orbit observations," *IEEE Trans. Geosci. Remote Sens.*, vol. 54, no. 10, pp. 6035–6047, Oct. 2016, doi: 10.1109/TGRS.2016.2580459.
[42] A. Bringer et al., "Properties of the RFI environment at 1400–1427 MHz as observed by the soil moisture active/passive mission microwave radiometer," *IEEE J. Sel. Topics Appl. Earth Observ. Remote Sens.*, vol. 14, pp. 7259–7267, 2021, doi: 10.1109/JSTARS.2021.3092996.
[43] P. A. Hwang, "Surface foam and L-band microwave radiometer measurements in high winds," *IEEE Trans. Geosci. Remote Sens.*, vol. 57, no. 5, pp. 2766–2776, May 2019, doi: 10.1109/TGRS.2018.2876972.
[44] T. Meissner and F. J. Wentz, "The emissivity of the ocean surface between 6 and 90 GHz over a large range of wind speeds and earth incidence angles," *IEEE Trans. Geosci. Remote Sens.*, vol. 50, no. 8, pp. 3004–3026, Aug. 2012, doi: 10.1109/TGRS.2011.2179662.
[45] L. Klein and C. Swift, "An improved model for the dielectric constant of sea water at microwave frequencies," *IEEE Trans. Antennas Propag.*, vol. 25, no. 1, pp. 104–111, Jan. 1977, doi: 10.1109/TAP.1977.1141539.
[46] S. H. Yueh, R. Kwok, and S. V. Nghiem, "Polarimetric scattering and emission properties of targets with reflection symmetry," *Radio Sci.*, vol. 29, no. 6, pp. 1409–1420, Dec. 1994, doi: 10.1029/94RS02228.
[47] K. He, X. Zhang, S. Ren, and J. Sun, "Delving deep into rectifiers: Surpassing human-level performance on imagenet classification," in *Proc. IEEE Int. Conf. Comput. Vis.*, 2015, pp. 1026–1034.
[48] C. Mears et al., "Improving the accuracy of the cross-calibrated multiplatform (CCMP) ocean vector winds," *Remote Sens.*, vol. 14, no. 17, pp. 4230–4244, Aug. 2022, doi: 10.3390/rs14174230.
[49] J. Boutin et al., "Correcting sea surface temperature spurious effects in salinity retrieved from spaceborne L-band radiometer measurements," *IEEE Trans. Geosci. Remote Sens.*, vol. 59, no. 9, pp. 7256–7269, Sep. 2021, doi: 10.1109/TGRS.2020.3030488.
[50] E. Jang et al., "Global sea surface salinity via the synergistic use of SMAP satellite and HYCOM data based on machine learning," *Remote Sens. Environ.*, vol. 273, May 2022, Art. no. 112980, doi: 10.1016/j.rse.2022.112980.

Xuchen Jin (Member, IEEE) received the Ph.D. degree in remote sensing from Zhejiang University, Hangzhou, China, in 2022.

He is currently a Postdoctoral Research Associate with the Southern Marine Science and Engineering Guangdong Laboratory, Guangzhou, China. He is also with the State Key Laboratory of Satellite Ocean Environment Dynamics, Second Institute of Oceanography, Ministry of Natural Resources, Hangzhou, China. His research interests include microwave remote sensing and radiative transfer in the coupled ocean and atmosphere system.

Xianqiang He received the B.S. degree in marine and ocean engineering from the Huazhong University of Science and Technology, Wuhan, China, in 1999, the M.S. degree in physical oceanography from the Second Institute of Oceanography, MNR, Hangzhou, China, in 2002, and the Ph.D. degree in physical electronics from the Shanghai Institute of Technical Physics, Chinese Academy of Sciences, Shanghai, China, in 2007.

He is currently with the State Key Laboratory of Satellite Ocean Environment Dynamics, Second Institute of Oceanography, MNR. He is also currently with the Ocean College, Zhejiang University, Hangzhou, China. His research areas of interest include radiative transfer in the coupled ocean and atmosphere system, atmospheric correction of satellite ocean color remote sensing, and oceanography research using ocean color remote sensing data.

Palanisamy Shanmugam received the Ph.D. degree in optical/microwave remote sensing techniques from Anna University, Chennai, India, in 2002.

He is currently a Professor/National Geospatial Chair Professor with the Department of Ocean Engineering, IIT Madras, Chennai. He has been a Principal Investigator of several projects funded by the Government of India. His research interests include ocean optics and imaging, satellite oceanography, radiative transfer in the ocean, algorithm/model development, and underwater wireless optical communication.

Jianyun Ying received the M.S. degree in physical oceanography from Hohai University, Nanjing, China, in 2013.

He is currently a Senior Engineer with the Laboratory of Ocean Engineer, Second Institute of Oceanography, Ministry of Natural Resources, Hangzhou, China. His research interests include marine hydrology and hydrodynamics.

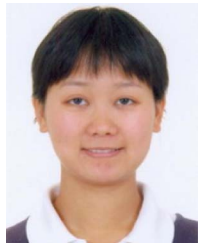

Fang Gong received the B.S. degree in computer and application from the Nanjing University of Information Science and Technology, Nanjing, China, in 2001.

She is currently a Senior Engineer with the State Key Laboratory of Satellite Ocean Environment Dynamics, Second Institute of Oceanography, MNR, Hangzhou, China. Her research interests include satellite data processing and analysis for ocean environment monitoring in open-ocean and near shore waters.

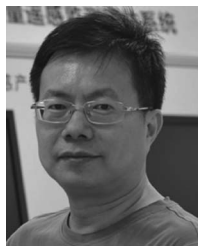

Qiankun Zhu received the B.S. degree in computer and application from the Ocean University of China, Qingdao, China, in 1997.

He is currently a Senior Engineer with the State Key Laboratory of Satellite Ocean Environment Dynamics, Second Institute of Oceanography, MNR, Hangzhou, China. His research interests include satellite data processing and ocean environment monitoring.

Delu Pan received the B.S. degree in physics from the Nanjing University of Science and Technology, Nanjing, China.

He is currently a Senior Scientist (expert of marine remote sensing) with the Second Institute of Oceanography, State Oceanic Administration, Hangzhou, China. He is also currently an Academician of the Chinese Academy of Engineering, Beijing, China, and a Professor with Zhejiang University, Hangzhou, China.

Prof. Pan is the Vice President of the Chinese Society of Oceanography and has been a member of the International Ocean Color Coordinating Group since 2000. He is the Editor-in-Chief of *Acta Oceanologica Sinica* (a journal of the Chinese Society of Oceanography).